Radar observations of the kinematic, microphysical, and precipitation characteristics of two MCSs in TRMM LBA

Robert Cifelli, Walter A. Petersen, Lawrence D. Carey, and Steven A. Rutledge
Department of Atmospheric Science, Colorado State University, Fort Collins, Colorado, USA

Maria A. F. da Silva Dias
Department of Atmospheric Science, University of São Paulo, São Paulo, Brazil

Received 15 December 2000; revised 9 August 2001; accepted 13 August 2001; published 25 September 2002.

[1] Dual-Doppler and polarimetric radar observations are used to analyze two mesoscale convective systems (MCSs) that occurred during the Tropical Rainfall Measuring Mission Large-Scale Biosphere-Atmosphere field campaign. The MCSs formed in different meteorological regimes, based on profiles of atmospheric wind and thermodynamic data. The first MCS event (26 January 1999) was a squall line that formed in low-level easterly flow and had an intense leading line of convection. In contrast, the 25 February 1999 MCS formed in low-level westerly flow and was best characterized by stratiform precipitation with embedded convective elements. The radar analyses suggest that the MCSs were distinct in terms of overall vertical structure characteristics. In particular, polarimetric radar cross sections indicated the presence of an active mixed phase zone in the easterly MCS that was largely absent in the westerly case. The easterly MCS had considerably more precipitation ice in the middle to upper troposphere compared to the westerly MCS. Composite analyses showed that the easterly MCS had higher peak reflectivities and a smaller reflectivity gradient above the 0°C level in convective regions of the storm compared to the westerly MCS event. Moreover, mean profiles of both vertical air motion and vertical mass transport in the convective portion of the easterly MCS were larger (over a factor of 2 at some heights below the 0° C level) than those in the westerly event. These observations suggest that the easterly and westerly wind regimes in the southwest Amazon region produce convection with different vertical structure characteristics, similar to regimes elsewhere in the global tropics (e.g., maritime continent). *INDEX TERMS:* 3314 Meteorology and Atmospheric Dynamics: Convective processes; 3329 Meteorology and Atmospheric Dynamics: Mesoscale meteorology; 3354 Meteorology and Atmospheric Dynamics: Precipitation (1854); 3374 Meteorology and Atmospheric Dynamics: Tropical meteorology *KEYWORDS:* Microphysics, tropical, precipitation, polarimetric radar, mesoscale convective system

Citation: Cifelli R., W. A. Petersen, L. D. Carey, S. A. Rutledge, and M. A. F. da Silva Dias, Radar observations of the kinematic, microphysical, and precipitation characteristics of two MCSs in TRMM LBA, *J. Geophys. Res.*, *107*(D20), 8077, doi:10.1029/2000JD000264, 2002.

1. Introduction

[2] A number of studies have shown that the global circulation is sensitive to the vertical distribution of heating associated with tropical mesoscale convective systems (MCSs) [*Hartmann et al*., 1984; *DeMaria*, 1985; *Gandu and Silva Dias*, 1998]. The distribution of heating in MCSs, involving both convective and stratiform processes, is largely driven by phase changes of water [*Houze*, 1989; *Tao et al*., 1993], which are in turn strongly coupled to the kinematic properties of MCSs [*Houze*, 1982; *Johnson and Young*, 1983; *Lin and Johnson*, 1994]. Thus both the vertical structure of hydrometeors and the kinematic quantities such as horizontal divergence, vertical air motion, and vertical mass flux can yield important information on the corresponding location of latent heat release [*Tao et al*., 1993; *Mapes and Houze*, 1995; *Kummerow et al*., 1996; *Olson et al*., 1999; *Yang and Smith*, 1999].

0148-0227/02/2000JD000264$09.00

[3] Characterization of the vertical structure of convection and the corresponding latent heating distribution in tropical convection is a major objective of the NASA Tropical Rainfall Measuring Mission (TRMM) [*Simpson et al*., 1988] program. To support TRMM, a series of field campaigns were conducted to provide detailed information on tropical convection in various locations. One of these experiments, the Tropical Rainfall Measuring Mission Large-Scale Biosphere-Atmosphere (TRMM LBA) experiment in Amazonia, was conducted in the Amazon region to provide detailed information on precipitation characteristics in the interior of a tropical continent. Information from TRMM LBA will be used for validation of TRMM satellite products and for initialization/validation of cloud models and passive microwave retrieval algorithms (used to estimate latent heating).

[4] The TRMM-LBA field experiment was conducted in the southwestern Amazon (state of Rondônia, Brazil) from 10 January to 28 February 1999. A variety of instrumentation was deployed during the field campaign, including airborne plat-

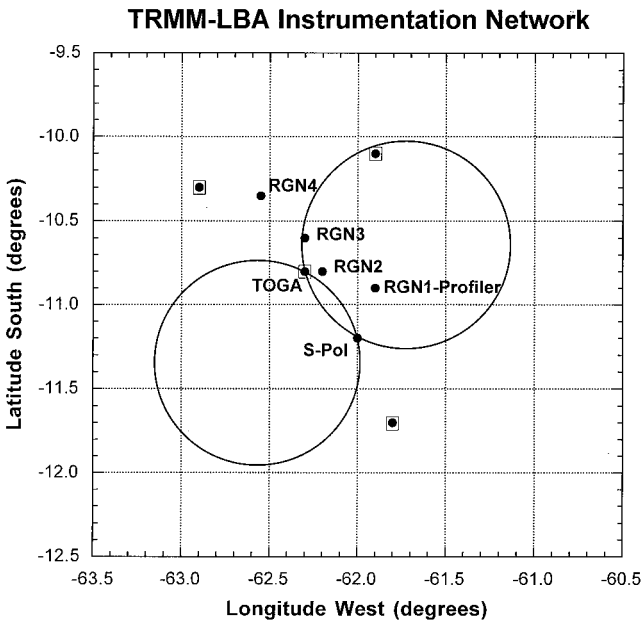

Figure 1. Map of selected instrumentation deployed in TRMM LBA. Circles indicate approximate location of the dual-Doppler radar lobes. RGN refers to Rain Gauge Network. Squared circles denote upper air sounding stations.

forms (University of North Dakota Citation and NASA ER-2) with microphysical, radar, and passive microwave instrumentation; atmospheric sounding stations; a boundary layer tethersonde and meteorological tower; rain gauge networks and disdrometers; precipitation profilers; and ground-based C-band Doppler (NASA TOGA) and S-band polarimetric (NCAR S-pol) radars (Figure 1). TRMM LBA was conducted in parallel with the WETAMC-LBA campaign [*Silva Dias et al*., 2002] aimed at examining the effect of land use change on rainfall in Amazonia.

[5] Climatologies addressing the vertical structure of convection across the global tropics have been made by a number of investigators [*Zipser*; 1994; *Zipser and Lutz*, 1994; *Petersen and Rutledge*, 1998, 2001; *Nesbitt et al*., 2000]. However, with the exception of a few well-studied locations such as the maritime continent [*Rutledge et al*., 1992; *Williams et al*., 1992; *Cifelli and Rutledge*, 1998; *Ahijevych et al*., 2000; *Carey and Rutledge*, 2000], the west Pacific [*Mapes and Houze*, 1995; *Demott and Rutledge*, 1998a, 1998b; *Rickenbach and Rutledge*, 1998], and the east Atlantic [*Cheng and Houze*, 1979], the variability of convection at a given location within a given season is not well understood. This work takes a step in that direction by examining differences in the vertical structure of two Amazonian MCSs sampled in distinct meteorological regimes during TRMM LBA using dual-Doppler and polarimetric radar analyses.

[6] A number of previous studies have examined characteristics of eastern Amazonian convection. Using satellite imagery, *Kousky* [1980] and *Molion* [1987] described the origin and inland propagation characteristics of squall lines originating along the northeast Brazilian coastline. These studies showed that Amazon coastal squall lines (ACSLs) can extend over 1000 km in length and last for periods up to 48 hours as they propagate inland across the Amazon region.

[7] *Greco et al*. [1990, 1994] and *Garstang et al*. [1994] used a combination of satellite imagery, a radiosonde network, and surface mesonet data to describe different types of squall line MCSs that were observed during ABLE 2B (Amazon Boundary Layer Experiment) [*Harriss et al*., 1990; *Garstang et al*., 1990]. The *Greco et al*. [1990] study showed that the Amazon region is influenced by coastally occurring systems (COSs), basin occurring systems (BOSs), and locally occurring systems (LOSs), depending on the origin location of the MCS. These systems were shown to have different diurnal characteristics over the ABLE 2B network: BOS produced most rainfall between 1000 and 1400 UTC, COS 1400 and 1800 UTC, and LOSs were most prolific after 1600 UTC. The BOS and COS produced the largest total rainfall totals, in agreement with surface divergence and mass inflow calculated from surface mesonet stations.

[8] *Garstang et al*. [1994] and *Greco et al*. [1994] described the kinematic and heat and moisture characteristics of selected COS (analogous to ACSL) using GOES satellite imagery in conjunction with radiosonde and mesonet surface data from a 1000 km^2 triangle network in ABLE 2B. A 3 cm radar was used in these studies to track echo features over the ABLE 2B network; however, the radar was of limited value in describing the vertical structure and rainfall characteristics due to severe attenuation in heavily raining cells. These studies described the different life cycle stages of an ACSL as well as their effect on the near-surface boundary layer. Moreover, profiles of divergence, vertical air motion (omega), and heat-moisture transports were constructed for both the leading edge convection (LEC) and the trailing stratiform region (TSR) components. The results showed that the stratiform anvil regions of the ACSLs were dynamically active and that both the LEC and the TSR made significant contributions to the total heat transport. (Similar conclusions regarding the relative contributions of convective and stratiform regions to the total heat budget of an ABLE 2B squall line were obtained by *Scala et al*. [1990] using a two-dimensional cloud model.) The kinematic profiles were consistent with similar profiles from other tropical locations [e.g., *Houze*, 1989]; however, the coarse resolution of the sounding data did not allow for a detailed analysis of the ACSL vertical structure.

[9] In this study we emphasize the detailed kinematic and microphysical characteristics observed in two convective systems in a different region of the Amazon Basin. This analysis is set in the framework of "large-scale forcing" by identifying the selected case studies as having occurred in distinct wind and thermodynamic meteorological regimes.

[10] The analysis takes advantage of the high-resolution dual-Doppler and S-band polarimetric radar data to characterize the vertical structure of the MCSs. Section 2 presents an overview of the radar methodologies used in the analysis. A brief discussion of the meteorological regimes observed during TRMM LBA is presented in section 3. Results, from both individual cross sections and composites, are discussed in section 4. Summary and conclusions are provided in section 5.

2. Methodology

2.1 Radar QC and Dual-Doppler Procedure

[11] During TRMM LBA the NASA TOGA radar and the NCAR S-pol radar were located 62 km apart in a mixed forest and deforested region of Rondõnia, Brazil (Figure 1). The radars employed several different scanning strategies during the field campaign, depending on whether aircraft were flying,

convection was occurring over one or more of the rain gauge networks, the height of the echo of interest, and/or whether the echo of interest was located in one or both of the dual-Doppler lobes. For this study, synchronized radar volume scan data within at least one of the dual-Doppler lobes was used for the dual-Doppler and polarimetric radar analyses. Each radar volume scan took ~ 4–7 min to complete, depending on the width of the sector region that was being sampled. The start time of the volume scans from each radar were typically synchronized within 30 s (details on the radar scanning strategy utilized during TRMM LBA can be found at http://radarmet.atmos.colostate.edu/lba_trmm/rad_scan.html).

[12] The TOGA radar measured reflectivity (Z), Doppler velocity (VR), and spectral width (SW), while the S-pol radar collected additional polarimetric variables, including differential reflectivity (Z_{DR}), linear depolarization ratio (LDR), total differential phase (Ψ_{DP}), and zero lag correlation coefficient between copolar horizontal and vertical polarized electromagnetic waves (ρ_{HV}) (see *Rogers* [1984], *Fulton and Heymsfield* [1991], *Herzegh and Jameson* [1992], *Doviak and Zrnic'* [1993], and *Straka et al*. [2000] for a discussion of these polarimetric variables). As discussed in the above references, multiparameter radar variables provide information on the size, shape, orientation, and thermodynamic phase in the sampling volume. When used together, these measureables can be used to characterize the predominant precipitation type in a radar resolution volume. For our two cases a total of 34 radar volumes were processed and analyzed (15 for 26 January and 19 for 25 February), as described below. The selected radar volumes spanned a continuous 2.5 hour period for the easterly event and 3.0 hour period for the westerly event at 10 min temporal resolution.

[13] Prior to unfolding radial velocities, the S-pol data were processed to eliminate ground clutter using thresholds in ρ_{HV} and the standard deviation of Ψ_{DP} [*Ryzhkov and Zrnic'*, 1998] and to calculate specific differential phase (K_{DP}) from the total differential phase (Ψ_{DP}) data as described by *Hubbert and Bringi* [1995] and *Carey et al*. [2000a]. To correct for propagation effects caused by precipitation at S-band, we implemented the mean procedure outlined by *Carey et al*. [2000a], which utilizes the differential propagation phase. This is a modification of the original *Ryzhkov and Zrnic'* [1995] technique for S-band data. Beam blockage by surrounding terrrain affected a portion of the southwest-northwest S-poI sampling area at the lowest tilt angle. Rain rates could not be reliably determined in a small portion of the grid where complete blockage of the radar beam occurred (4° sector from 258° to 261°). In regions where the beam blockage was only partial (an approximate 90° sector extending southwest-northwest of S-pol), reliable estimates of the rain rate could still be obtained using K_{DP}, which is immune to partial beam blocking [*Zrnic' and Ryzhkov*, 1996], or a corrected value of horizontal reflectivity (Z_H) (see Figure 2). The horizontal reflectivity was corrected for partial blocking by analyzing the azimuthal trend of Z_H that satisfied $1° < K_{DP} < 2°$ km^{-1}. Independent of blocking effects, this threshold results in a fixed range in Z_H [*Balakrishnan and Zrnic'*, 1990]. Any bias below this fixed range was attributed to partial blocking and was removed by adding the necessary offset (see *Carey et al*. [2000b] for details on the rainfall estimation procedure).

[14] Radial velocity data from both TOGA and S-pol were manually unfolded using the NCAR RDSS (Research Data Support System) software [*Oye and Carbone*, 1981]. The unfolded data were interpolated onto a 1.0 km horizontal resolution and a 0.5 km vertical resolution Cartesian grid centered on the S-pol radar using the NCAR REORDER software package [*Mohr et al*., 1986]. The areal extent of the Cartesian grids were similar: 16,000 km^2 for 26 January and 15,000 km^2 for 25 February. The grids were made as large as possible in order to evaluate the impact of the MCSs on the large scale.

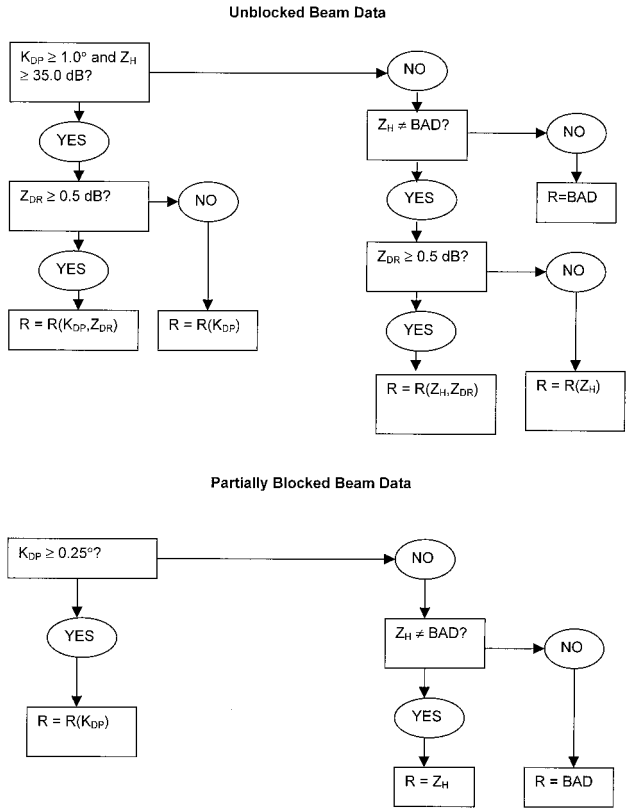

Figure 2. Decision tree algorithm to determine which polarimetric estimator is used to calculate rain rate for a specific grid point. The rain rate estimator equations are shown in Table 1.

[15] Dual-Doppler analyses were performed using the NCAR CEDRIC (Custom Editing and Display of Reduced Information in Cartesian Space) software package [*Mohr and Miller*, 1983]. The S-poI data were used for estimating reflectivity-weighted fall speed in the synthesis since the S-pol radar was subject to less attenuation than the C-band TOGA radar and was corrected for propagation effects. An average storm motion vector was calculated for each event to perform a differential advection in the synthesis. The storm motion vector was determined by inspection of the leading edge of the convection in sequential low-level reflectivity CAPPIs. A one-step Leise filter and patching function were applied to the horizontal winds one time after the initial synthesis in order to remove spurious data and smooth the resulting u,v wind field. Vertical air motion (w) in each synthesis volume was calculated by setting the top boundary 0.25 km above the highest measured divergence in each grid column, setting w=0 at this level, and integrating downward to the lowest grid height of 0.5 km above ground level (agl). A variational adjustment scheme [i.e., *O'Brien*, 1970] to redistribute residual mass was not utilized because a reliable lower boundary condition for vertical air motion across the entire domain could not be determined.

Comparisons of selected vertical air motion profiles with similar profiles using a variational adjustment scheme showed minimal difference in terms of the overall structure of the vertical air motion profile. Moreover, the vertical air motion profiles, retrieved from the downward integration procedure, were compared with in situ aircraft measurements sampled in the 26 January event as well as with multiple Doppler synthesis from the EDOP radar on the NASA ER-2 aircraft for a different TRMM-LBA event (not shown). In both cases the ground radar vertical air motion estimates were in good agreement (i.e., within 1–2 m s^{-1}) with the estimates from independent aircraft platforms.

2.2. Partitioning Algorithm

[16] A partitioning algorithm, based on *Rickenbach and Rutledge* [1998] and *Steiner et al*. [1995], was used to separate areas of convection from nonconvective regions for each synthesized radar volume. This technique examines the spatial uniformity and intensity of a low-level map of radar reflectivity (i.e., 2 km height) to delineate areas of horizontally variable precipitation (convective rainfall) from weaker, horizontally uniform precipitation (decaying convection and stratiform rainfall). The partitioned reflectivity fields were examined subjectively for several individual volumes to evaluate the performance of the algorithm. It was found that the algorithm performed well in terms of isolating the intense convective cells from the surrounding reflectivity field; however, it was often observed that decaying or weak convective echo was classified together with more typical stratiform precipitation regions. Therefore we refer to this partitioned precipitation category as weak convective-stratiform (WCSF) in order to emphasize that it represents a mixture of decaying convection (no bright band signature) as well as stratiform echo features.

2.3. Hydrometeor Characteristics From Polarimetric Observables

[17] In this study, a comparison of polarimetric radar-derived precipitation characteristics, including precipitation ice mass and precipitation liquid water content, was made using procedures similar to those outlined by *Carey and Rutledge* [2000]. The precipitation characteristics were determined over the same horizontal grid as the dual-Doppler data. As described by *Carey and Rutledge* [2000], a difference reflectivity (Z_{dp}) method [*Golestani et al*., 1989] was used to discriminate horizontally polarized reflectivity (Z_H) for rain and ice. If the Z_{dp} method indicates the presence of mixed phase precipitation, then estimates of rain mass (M_w) and ice mass (M_i) are calculated using the following *Z-M* relationships for liquid and ice water:

$$M_w = 3.44 \times 10^{-3}[Z_H^{\text{rain}}]^{(4/7)}\ (\text{g m}^{-3})\,, \tag{1}$$

where Z_H^{rain} is in $\text{mm}^6\ \text{m}^{-3}$ [*Ryzhkov and Zrnic'*, 1995] and

$$M_{\text{ice}} = 1000\pi\rho_i N_0^{3/7}\left(\frac{5.28 \times 10^{-18} Z_H^{\text{ice}}}{720}\right)^{4/7}\ (\text{g m}^{-3}), \tag{2}$$

where Z_H (ice) is in $\text{mm}^6\ \text{m}^{-3}$, ρ_i is the ice density (0.917 kg m^{-3}), and N_0 ($4 \times 10^6\ \text{m}^{-4}$) is the intercept parameter of an assumed inverse exponential distribution for ice (see *Carey and Rutledge* [2000] for details on the M_{ice} relationship). If the Z_{dp} method indicates the presence of pure rainwater (if the difference between the observed horizontal reflectivity (Z_H) and the estimated reflectivity associated with rain ($Z_H^{\text{rain}}(Z_{dp})$) is less than the standard error (1.1 dB), then it is assumed that reflectivity is dominated by water and equation (3) is utilized; also, the standard error is multiplied by a constant which gets larger (linearly) with increased distance below the melt level; this is done to make the threshold for ice detection below the melt level more restrictive at distances closer to the ground), then M_w is calculated from

$$M_w = 0.70 \times 10^{-3}(Z_H^{0.886})(\varsigma^{-4.159})\ (\text{g m}^{-3})\,, \tag{3}$$

where Z_H (Z_V) is the observed reflectivity at horizontal (vertical) incidence in $\text{mm}^6\ \text{m}^{-3}$ and [*Bringi and Chandrasekar*, 2001]

$$\varsigma = \frac{Z_H}{Z_V} = 10^{Z_{DR}/10}. \tag{4}$$

If the Z_{dp} method indicates the presence of pure ice, then (2) is utilized with $Z_H^{\text{ice}} = Z_H^{\text{observed}}$.

[18] The ice and liquid water contents reported herein are only approximate since a number of assumptions concerning hydrometeor shapes and size distributions were used to develop the *Z-M* relations [*Carey and Rutledge*, 2000]. However, because our goal is to examine the relative trends in ice-liquid content between the two MCSs in a statistical sense as opposed to analyzing the absolute magnitude at any particular grid point, the relationships were deemed appropriate for this study

[19] Mass-weighted mean diameter for liquid drops is calculated on the basis of the relation [*Bringi and Chandrasekar*, 2000]

$$D_m = 1.619\ *\ Z_{DR}^{(0.485)}. \tag{5}$$

D_m is only calculated if the quantity ($Z_H^{\text{observed}} - Z_H^{\text{rain}}$) is less than the standard error (1.1 dB) of Z_H^{rain} from the Z_{DP} method. Rain rates were calculated subsequent to interpolating the S-pol surveillance scan data (two tilt scans, 0.5°–0.7° and 1.1°–1.5°) to a 40,000 km^2 CAPPI (1 km height) grid with 2 km resolution centered on the location of the S-pol radar. The temporal resolution of the resulting rain map was ~10 min and bracketed the time period of dual-Doppler observations for each event.

[20] The rain rates for each radar volume were calculated using an optimization technique with the parameters Z_H, Z_{DR}, and K_{DP} [*Chandrasekar et al*., 1993; *Petersen et al*., 1999; *Carey and Rutledge*, 2000, Appendix D]. The rainfall estimators for each grid point are chosen on the basis of thresholds which maximize the measurement capability of each polarimetric variable (i.e., minimize the rain rate standard error) and combinations of those variables in rain rate equations as described

Table 1. Polarimetric Radar Rain Rate Estimators[a]

Equation	Unit
(1) $R(K_{DP}, Z_{DR}) = 87.6 \cdot (K_{DP})^{0.934} \cdot (10)^{(0.1\ \cdot\ -1.59\ \cdot\ Z_{DR})}$	mm h^{-1}
(2) $R(Z_H, Z_{DR}) = 6.70 \times 10^{-3} \cdot (Z_H)^{0.927} \cdot (10)^{(0.1\ \cdot\ -3.433\ \cdot\ Z_{DR})}$	mm h^{-1}
(3) $R(K_{DP}) = 53.8 \cdot (K_{DP})^{0.85}$	mm h^{-1}
(4) $R(Z_H) = 0.02180 \cdot (Z_H)^{0.70}$	mm h^{-1}

[a]Units: K_{DP}, ° km^{-1}; Z_{DR}, dB; and Z_H, $\text{mm}^6\ \text{m}^{-3}$. Equations (1), (2), and (3) were taken from *Bringi and Chandrasekar* [2000]. Equation (4) was derived from TRMM-LBA disdrometer data by A. Tokay (personal communication, 2000).

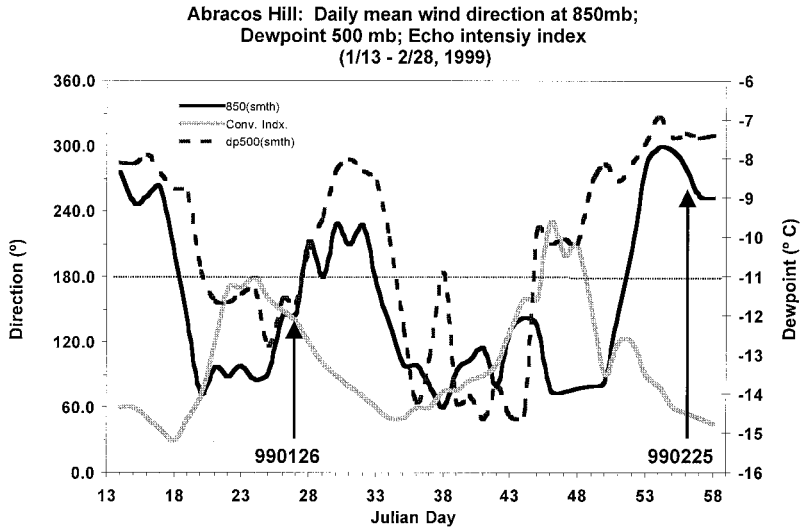

Figure 3. Time series of 850 mbar smoothed wind direction (black solid line) and 500 mbar dew point temperature (dashed line) from the Abracos Hill sounding site near the TOGA radar. The convective index (gray solid line) represents a ratio of total 40 dBZ area coverage/10 dBZ area coverage using the TOGA radar data (time series courtesy of Dennis Boccippio). The convective index values range from ~ 0.003 to 0.02. A running mean has been applied to the time series. The time periods corresponding to the 26 January (990126) and 25 February (990225) MCSs are indicated.

in Figure 2. The rain rate relations for each polarimetric estimator are shown in Table 1.

3. Meteorological Regimes

[21] Several studies [*Rickenbach et al*., 2002; *Halverson et al*., 2001; *Rutledge et al*., 2000] showed that two primary meteorological regimes were observed during the TRMM LBA, based on the low-level (850 mbar) zonal wind component, westerly and easterly. The Rickenbach et al. study found these regimes to be modulated by changes in the large-scale flow patterns over South America. In particular, the Rickenbach et al. results suggest that the migration of the Bolivian High and trough over northeast Brazil modulate the upper level flow in Rondõnia and influence the extent to which stationary fronts penetrate into Amazonia. The modulation produces corresponding shifts in the low-level wind direction over the Amazon region.

[22] The westerly regime was characterized by low-level west to northwest flow and the presence of a relatively moist troposphere (Figure 3). During these westerly periods, convection appeared to be less vertically developed, exhibiting lower daily peak lightning flash rates [*Williams et al*., 2002; *Halverson et al*., 2001] and lower maximum rain rate intensity. (Despite the lower maximum rainfall intensity, precipitation during the westerly regime was slightly greater in terms of the mean, median, and total depth of precipitation as determined from S-pol radar statistics (not shown).) During the easterly regime, convection occurred in a slightly dryer troposphere coincident with low-level easterly flow. Convection during the easterly regime was typically more vertically developed. Consistent with the enhanced vertical development, visual observations of lightning, as well as data from the TRMM lightning imaging sensor (LIS) and the Brazil Lightning Detection Network (BLDN) [*Petersen et al*., 2001], flat plate antennas at the TOGA radar site [*Halverson et al*., 2001] show that easterly convection was typically highly electrified.

[23] Recognizing the potential implications for TRMM in terms of latent heating parameterization, we set out to explore, quantitatively, whether differences in the vertical structure of convection existed in these two regimes. Our results demonstrate that for the convection observed in the two MCSs examined in this study, the kinematic and microphysical differences are consistent with the regimes identified in the sounding wind and thermodynamic data.

4. Results

4.1. General Characteristics of Convection

[24] This section provides a brief overview of the evolution of the two MCS examined in this study.

4.1.1. 26 January Easterly MCS

[25] The 26 January event formed as a squall line with a leading line of convection and a trailing region of decaying convection and stratiform precipitation. Animation of Geostationary Observational Environmental Satellite (GOES) imagery showed that the line formed as an outflow boundary from previous convection several hundred kilometers northeast of the TRMM-LBA sampling domain. Further analysis of the GOES imagery showed that the convective system responsible for organizing the outflow boundary may have been associated with a large squall line that propagated from the northeastern Brazilian coast line the previous day (i.e., an ACSL) [*Garstang et al*., 1994]. However, the association is complicated by the fact the line of convection in this study was isolated from other regions of convection to the north and south and that this line appeared to interact with a separate boundary that moved in from the north (as noted in the GOES animations).

[26] The MCS entered the east dual-Doppler lobe (Figure 1) around 1950 UTC as a vigorous line of convection oriented approximately north-south with little trailing echo. The leading line was intense, with peak reflectivities exceeding 60 dBZ and

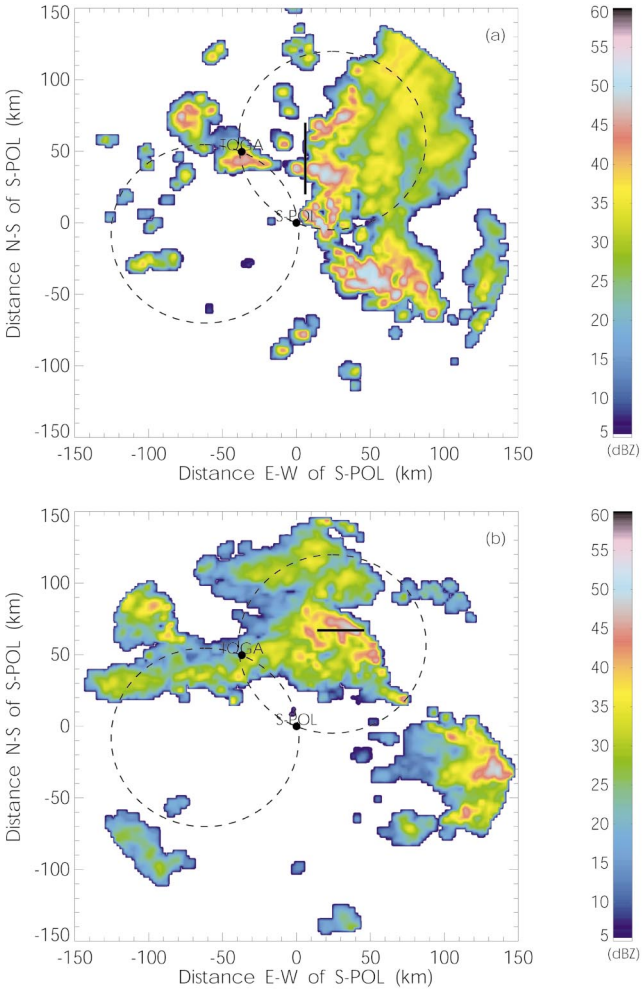

Figure 4. Radar CAPPIs of contoured reflectivity at 2 km agl for the 26 January easterly MCS at 2057 UTC and the 25 February westerly MCS at 2336 UTC. Approximate location of cross sections shown in Figures 6 and 7 are indicated by solid lines. Reflectivity scales (dBZ) are indicated in the right-hand portion of each plot.

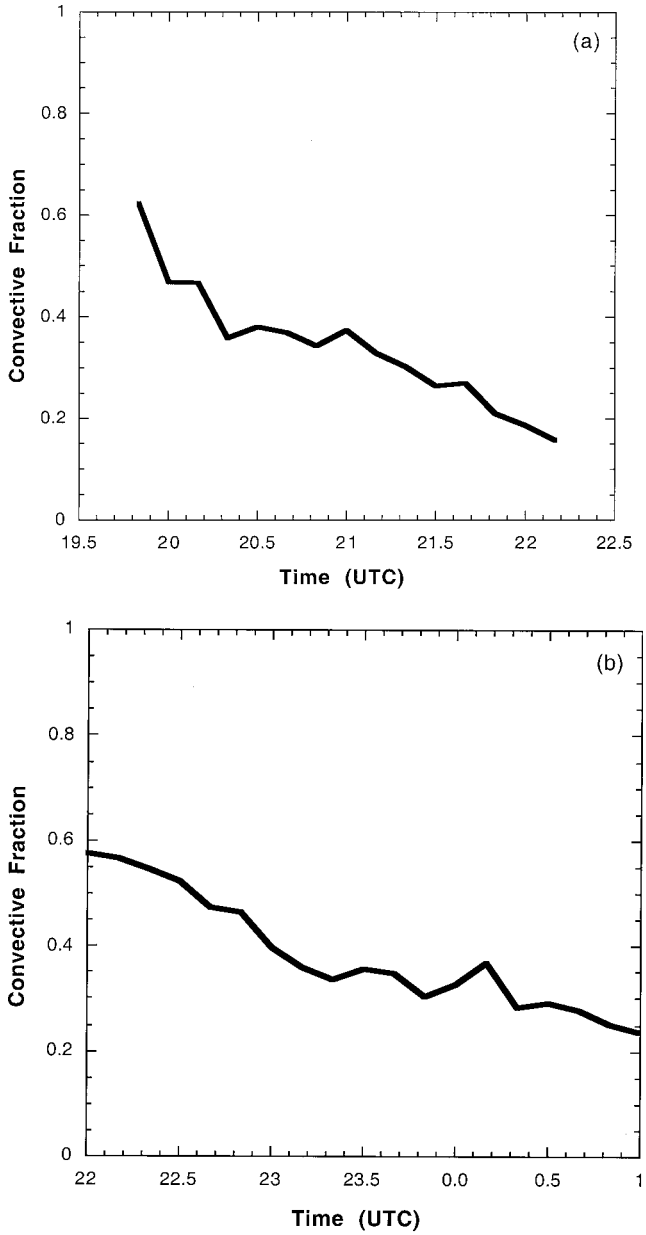

Figure 5. Time series of convective fraction (ratio of number of convective grid points to number of convective plus WCSF grid points) for (a) the 26 January easterly MCS and (b) 25 February westerly MCS as determined by the partitioning algorithm at a height of 2 km.

echo tops approaching 19 km agl. Peak updraft magnitudes were in excess of 20 m s^{-1} at this time. Inspection of radar CAPPI (constant altitude plan position indicator) plots showed that the 26 January MCS appeared to be transitioning from the intensifying to the mature stage (as defined by *Leary and Houze* [1979]). As the system moved westward across the dual-Doppler domain, the MCS developed a trailing region of stratiform and decaying convective precipitation and decreased in overall intensity. Around 2100 UTC the leading line merged with an east-west–oriented cell complex that had formed ahead of the line over the TOGA radar (Figure 4a). For this particular case, dual-Doppler syntheses were performed on radar volumes collected from 1950 to 2210 UTC.

4.1.2. 25 February Westerly MCS

[27] The 25 February MCS was one of a number of westerly regime MCSs that were sampled during late February in TRMM LBA. Its overall development appeared much more complex than the 26 January MCS. Radar animations showed that the MCS began as a cluster of cells located north of S-pol around 2000 UTC (16 L), probably in response to diurnal heating. Over the next several hours these cells grew in the northwest-southeast direction and many of the cells merged as the whole complex moved slowly to the east. For several hours during the dual-Doppler sampling period the MCS contained a broad arc of convective elements along its eastern margin (Figure 4b). However, the storm organization could best be characterized as a broad area of relatively homogeneous precipitation with apparently randomly oriented regions of embedded convection similar to monsoon convection observed in the maritime continent region of northern Australia [*Keenan and Carbone*, 1992; *Cifelli and Rutledge*, 1998]. The MCS remained in the dual-Doppler lobes for over 9 hours; however, it began to dissipate significantly after about 0200 UTC on 26 February. For this case, dual-Doppler syntheses were per-

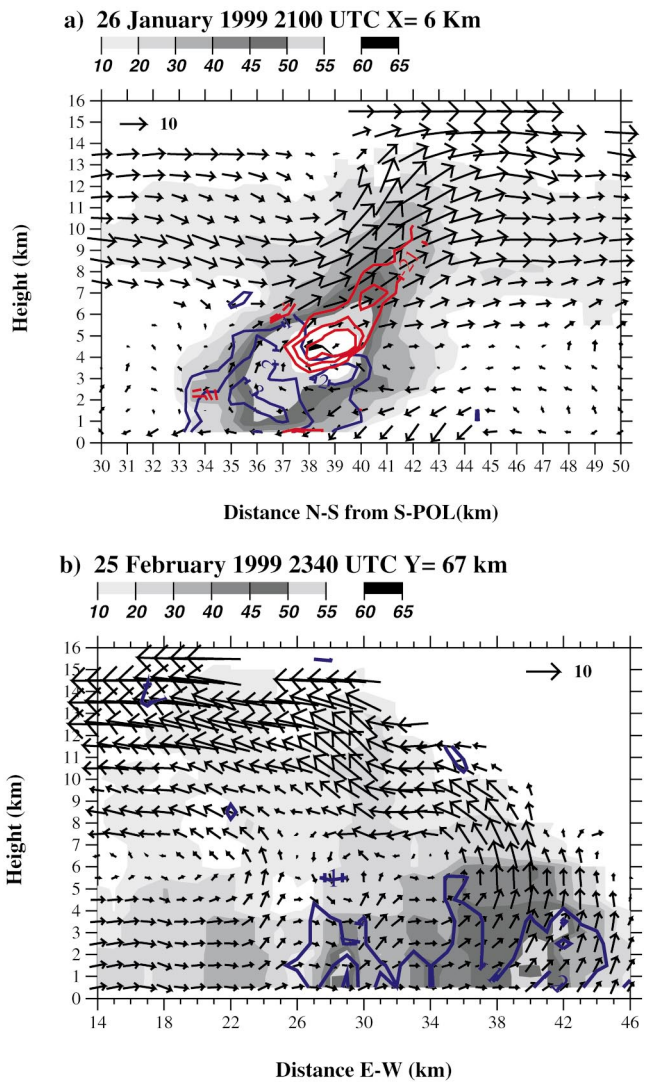

Figure 6. (a) North-south vertical cross section for the 26 January easterly MCS through a vigorous convective cell at 2100 UTC. Radar reflectivity is shaded as indicated, Z_{DR} is contoured in blue from 1 dB at an interval of 1dB. LDR is contoured in red for values of −23, −21, and −19 dB. Velocity vectors are plotted in a storm-relative framework (scale indicated in each figure). (b) As in Figure 6a except an east-west cross section for 25 February 1999, 2340 UTC (note strong LDR signals absent in this case). Approximate location of cross sections are indicated in Figure 4. The cross sections were constructed by superimposing dual-Doppler winds (interpolated onto a 1 km horizontal by 0.5 km vertical grid) with radar Z_H, Z_{DR}, and LDR (interpolated to a 0.5 km horizontal by 0.5 km vertical grid).

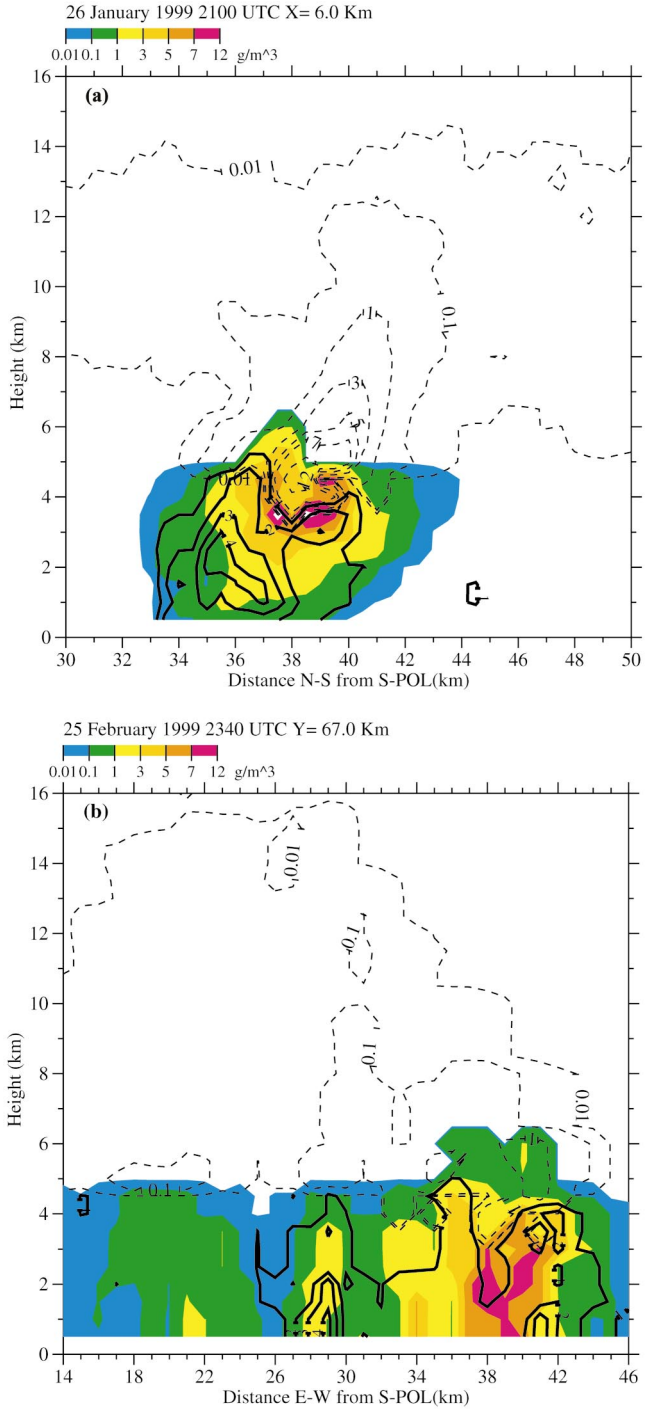

Figure 7. (a) Same as (Figure 6a) except rainwater content (g m^{-3}) (shaded as shown), precipitation ice water content (g m^{-3}) (dashed contours at 0.01, 0.1, 1, 3, 5, 7, and 12 g m^{-3}), and mass-weighted mean raindrop diameter (mm) (thick contour starting at 1 mm every 1 mm). (b) Same as (Figure 7a) except for the cross section shown in Figure 6b.

formed on radar volumes collected from 2200 UTC on 25 February to 0100 UTC on 26 February.

[28] Figure 5 shows the fraction of convective echo for each MCS during their respective sampling periods. These plots show that the MCSs had approximately the same fraction of convective echo during their respective sampling periods. Visual inspection of radar PPIs and CAPPIs suggest that both the 26 January and the 25 February MCSs were sampled primarily during their mature stage of evolution [*Leary and Houze*, 1979].

4.2. Storm Cross Sections

[29] Representative cross sections of the vector wind field, Z_H, Z_{DR}, and LDR are shown in Figure 6 for relatively intense convective cells sampled during the 26 January easterly MCS and the 25 February westerly MCS. For the easterly case, note the tilted updraft and corresponding Z_{DR} column extending

above 5 km, indicating an abundance of oblate drops (i.e., drops greater than 1.5–2.0 mm in diameter) being lofted into the mixed phase region. (Retrieved vertical air motions in this cross section are probably an underestimate of actual air motions due to the coarse resolution of the wind field compared to the polarimetric variables (see Figure 6)). Z_{DR} values exceeding 3 dB near the 2 km level suggest the presence of drops exceeding 4 mm in diameter (see also Figure 7a). The dip in the Z_{DR} contours in the weaker updraft region on the right-hand side of the cell in Figure 6a corresponds to an LDR enhancement, suggesting a hail production mechanism via the freezing and subsequent riming of millimeter-sized raindrops [e.g., *Goodman et al*., 1988; *Fulton and Heymsfield*, 1991; *Herzegh and Jameson*, 1992; *Takahashi and Kuhara*, 1993; *Ferrier et al*., 1995; *Bringi et al*., 1997; *Petersen et al*., 1999; *Smith et al*., 1999; *Carey and Rutledge*, 2000]. Some of the larger frozen drops probably fell back through the weaker updrafts on the northern fringe (right-hand side of cell in a) and melted, causing a local peak in rainwater content (see Figure 7a). The slight enhancement in LDR on the left side of the updraft above the main Z_{DR} column suggests that frozen drops and/or small hail and graupel particles rose in the updraft core and rimed [*Herzegh and Jameson*, 1992; *Fulton and Heymsfield*, 1991]. Figure 7a shows that the 26 January updraft was able to support an efficient collision-coalescence precipitation process, evidenced by the high liquid water contents and large drop diameters, as inferred from the polarimetric radar measurements. Note also the significant amount of ice being lofted into the middle and upper troposphere. The lofting of supercooled rainwater into the mixed phase zone and subsequent production of large amounts of precipitation ice via drop freezing is reminiscent of the polarimetrically derived precipitation structure of tropical island convection observed during MCTEX (Maritime Continent Thunderstorm Experiment) [e.g., *Ahijevych et al*., 2000; *Carey and Rutledge*, 2000].

[30] The contrasting cross sections for the 25 February MCS are shown in Figures 6b and 7b. The cross sections show significantly weaker updrafts in this cell and the complete absence of any LDR enhancement in the mixed phase region. Consistent with the weaker updrafts, there is a relatively sharp reflectivity gradient above the 0°C level (Figure 6b) and paucity of precipitation ice in the middle to upper troposphere (Figure 7b). While Z_{DR} columns and associated coalescence growth clearly exist in Figure 6b, this cross section shows an absence of robust mixed phase microphysics, in contrast to the 26 January MCS.

[31] These differences in hydrometeor vertical structure have important implications for TRMM algorithms designed to retrieve surface rainfall and latent heating characteristics from passive microwave signatures [e.g., *Kummerow et al*., 1996; *Olson et al*., 1999]. For example, the Goddard profiling algorithm (GPROF) currently utilizes a database of simulated hydrometeor profiles and associated upwelling brightness temperatures from tropical oceanic convection in order to determine the best match to a set of observed brightness temperatures [*Kummerow et al*., 1994a, 1994b, 1996], even for land-based retrievals. The performance of GPROF retrievals over land is often poor compared to over ocean due to the limited radiometric response over land and the increased reliance of the retrieval on the database of simulated hydrometeor profiles (C. Kummerow, personal communication, 2000). Future improvements in GPROF, especially over land areas, will require accurate simulated profiles of rain and ice for different geographic regions. These simulations of hydrometeor profiles can be validated against observations similar to those provided in this study.

4.3. Composite Vertical Structure

[32] In this section we examine the composite vertical structure of each MCS event and compare the salient characteristics. The comparison is made using both the contoured frequency by altitude diagram (CFAD) [*Yuter and Houze*, 1995] and the mean profiles. The CFADs are a convenient way to display multiple histograms in a two-dimensional format. At each height the CFAD displays the relative frequency of occurrence of a given parameter. Composite characteristics of each MCS are analyzed in sections 4.3.1 and 4.3.2 by partitioning reflectivity, vertical mass transport, and vertical air motion for each dual Doppler synthesis volume into convective and WCSF components, combining the data from all the volumes, and examining statistics for each precipitation category. Moreover, composite characteristics of water content, mass weighted mean drop diameter, and rainfall intensity are compared in sections 4.3.3 and 4.3.4. For the water content and rainfall comparisons no discrimination is made between convective and WCSF components of the MCSs.

4.3.1. Reflectivity

[33] The reflectivity CFAD and mean profile results are shown in Figure 8 for both easterly and westerly case studies. Comparison of the CFADs (top and middle rows of Figure 8) show that the easterly MCS has a significantly higher frequency of occurrence of intense echo features throughout the depth of the troposphere. For example, in the convective region the height at which the probability of occurrence of 30 dBZ echo falls below 1% is about 13 km for the easterly case (Figure 8a) compared to 8 km in the westerly case (Figure 8d). Previous results from the western Pacific warm pool region [*DeMott and Rutledge*, 1998a] indicate that rainfall production is larger for radar echoes with higher maximum 30 dBZ echo heights. Moreover, *Petersen and Rutledge* [2001] show a similar correlation for rainfall rates and 30 dBZ echo height across the global tropics using TRMM precipitation radar (PR) data. Thus the CFAD results in Figure 8 suggest that the easterly MCS would produce higher rain rates compared to the westerly MCS. As shown below in section 4.3.4, the easterly MCS did indeed produce significantly larger rainfall rates compared to the westerly MCS.

[34] Not surprisingly, the mean convective profiles (Figure 8g) show that the easterly system has a smaller vertical reflectivity gradient in the mixed-phase region (i.e., 4–8 km) in the convective region compared to the corresponding profile in the westerly event. The difference in the composite reflectivity gradients are consistent with the cross sections shown earlier which indicated an absence of large particles above the melting level (near 4.5 km agl) in the westerly case compared to the easterly MCS. The difference in mean convective profiles between the easterly and the westerly events is reminiscent of differences between break and monsoon convection observed in the maritime continent region of northern Australia [*Rutledge et al*., 1992; *Williams et al*., 1992; *Zipser and Lutz*, 1994; *Cifelli and Rutledge*, 1998]. Overall, the westerly composite reflectivity profile is similar to profiles observed in many previous studies of tropical oceanic convection [*Zipser et al*., 1981; *Szoke et al*., 1986; *Jorgensen and LeMone*, 1989; *Williams et al*., 1992; *Rutledge et al*., 1992; *Zipser and Lutz*, 1994; *DeMott and Rutledge*, 1998a], while the easterly profile appears more con-

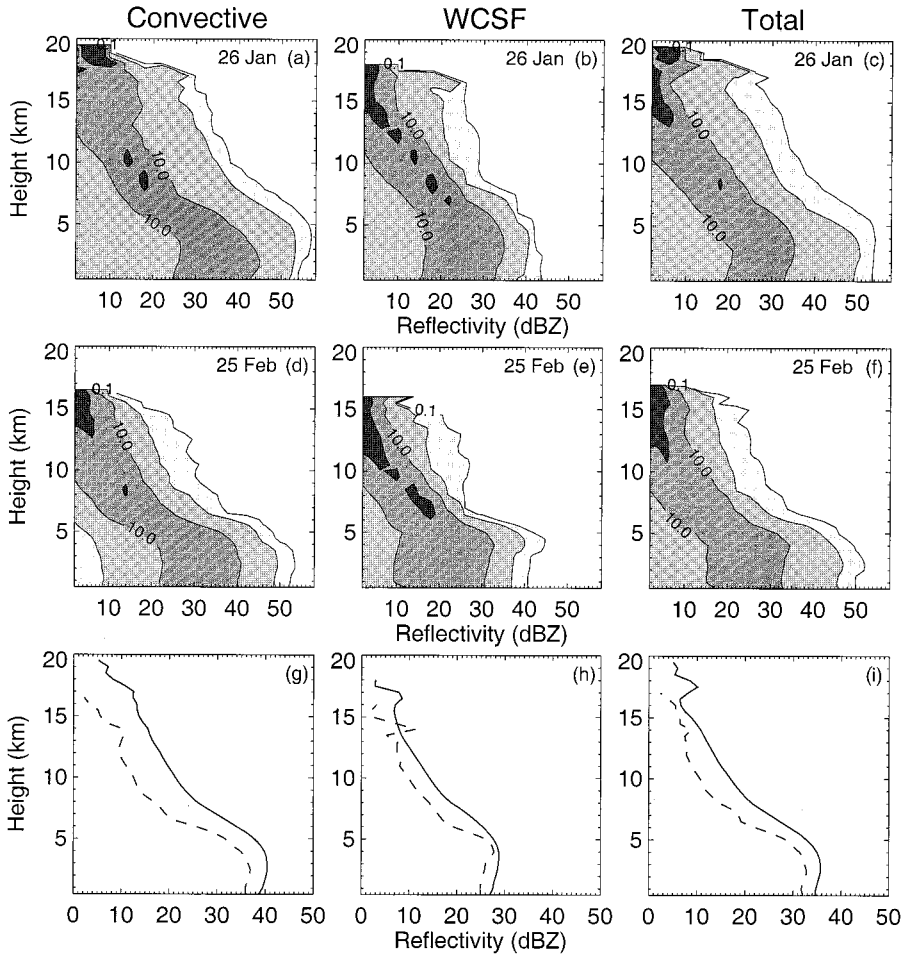

Figure 8. CFADs of radar (S-pol) reflectivity for the 26 January easterly (top, panels a-c) and 25 February westerly (middle, panels d-f) events. Panels (g-i) are mean profiles for 26 January (solid line) and 25 February (dashed line). Panels from left to right in all rows are for convective, WCSF, and total (convective plus WCSF) categories, respectively. CFAD contours are shaded with increasing darkness at the 0.1, 1.0, 10.0, and 30.0% relative frequency of occurrence. The CFADs were constructed using a 4 dB bin size and 15 total bins.

sistent with tropical continental profiles [*Rutledge et al*., 1992; *Williams et al*., 1992; *Zipser and Lutz*, 1994; *Cifelli and Rutledge*, 1994, 1998]. These results suggest that at least two convective regimes were sampled in the Amazon wet season during TRMM LBA: one that has characteristics similar to tropical continental convection (easterly) and one that has characteristics similar to tropical oceanic convection (westerly) [*Williams et al*., 2002]. These results may have important implications for diabatic heating profiles in numerical cloud models [*Tao et al*., 1990, 1993] as well as for retrieving the vertical distribution of hydrometors and surface rainfall using passive microwave algorithms [*Fulton and Heymsfield*, 1991; *Kummerow and Giglio*, 1994a, 1994b; *Kummerow et al*., 1996; *Olson et al*., 1999; *Yang and Smith*, 1999].

[35] The WCSF mean reflectivity profiles (Figure 8h) and CFADs (Figures 8b and 8e) also show some important differences in vertical structure. The 25 February MCS featured a pronounced bright band signature, suggesting the occurrence of stratiform microphysical processes. In contrast, the 26 January profile and CFAD do not show any evidence of a bright band. In fact, the WCSF vertical structure for the easterly event looks quite similar to the convective vertical structure, albeit with reduced intensity.

4.3.2. Vertical Air Motion and Mass Transport

[36] CFADs for vertical wind speed and mean profiles of vertical air motion are compared in Figure 9 for the easterly and westerly cases. The CFAD panels include contours of total vertical mass transport per vertical velocity bin, similar to *Yuter and Houze* [1995], in order to identify which vertical drafts are responsible for the majority of mass transport. With regard to the vertical velocity CFADs, note that the modes of the distributions are nearly identical for the MCSs within each precipitation category. The major difference is the fact that the tails of the vertical draft distributions are significantly wider for the easterly MCS versus the westerly MCS; that is, in the easterly case there is a higher relative frequency of occurrence of intense vertical velocity at all heights compared to the westerly case. The net effect of the difference at the tail of the distribution is to offset the magnitude of the mean profiles.

[37] In the convective region the mean vertical air motion profile (Figure 9g) for the easterly MCS has a larger magnitude throughout the depth of the troposphere. Specifically, the mean easterly MCS profile is more than a factor of 2 larger than the corresponding westerly profile between 1 and 2 km and 20–60% larger between 3 and 4 km. The large drafts in the

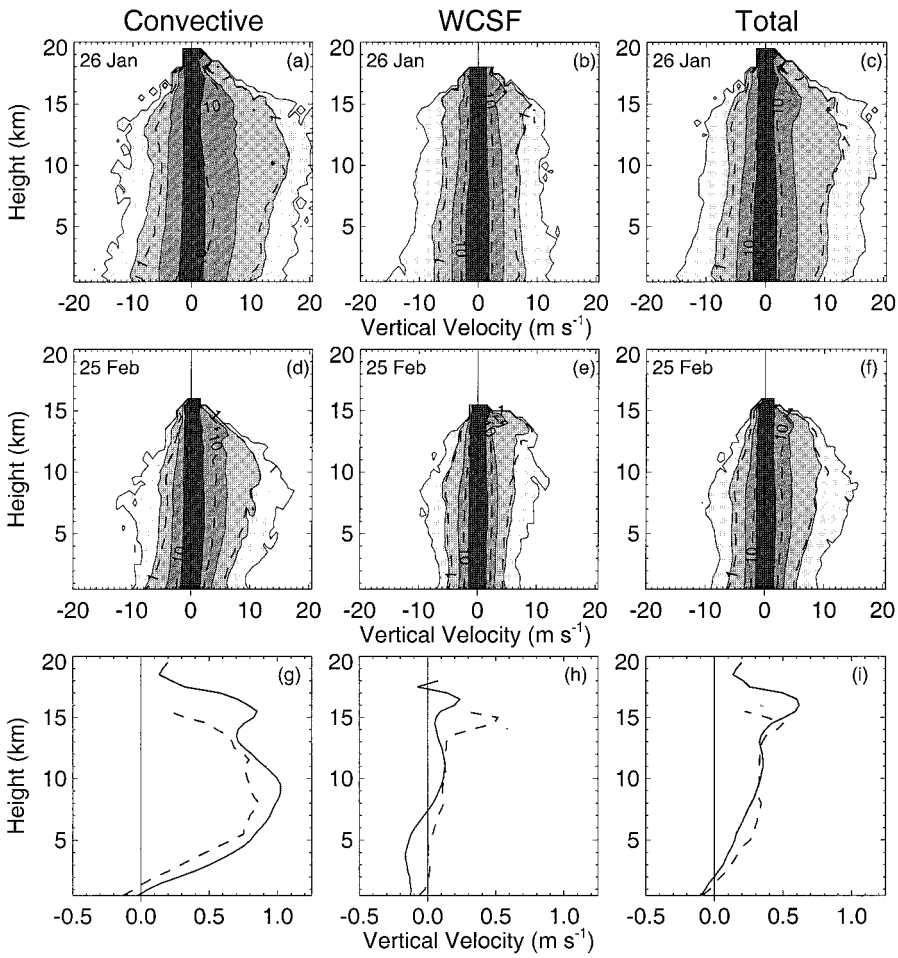

Figure 9. Same as Figure 8 except for vertical air motion with contours and shading at 0.01, 0.1, 1.0, and 10% relative frequency of occurrence. Dashed contours of mass transport per vertical velocity bin, expressed as a percentage of total mass transport for each height level, are included in the CFADs to identify which vertical drafts are responsible for the majority of the mass transport. The contours of the mass transport per vertical velocity bin are 1 and 10%. The vertical air motion CFADs were constructed using a 1 m s^{-1} bin size and 31 total bins. Note the change in scale in the bottom row panels (mean profiles) compared to top and middle rows (CFADs).

easterly MCS allow for a significant number of raindrops to be carried above the melt level and provide an important source of large ice particles and supercooled drops in this region [*Zipser and Lutz*, 1994; *Ferrier et al*., 1995; *Jameson et al*., 1996; *Bringi et al*., 1997; *Smith et al*., 1999; *Carey and Rutledge*, 2000], affecting the vertical distribution of hydrometeors in these MCSs.

[38] The differences in convective vertical air motion structure shown in Figure 9 are similar to differences observed in convective vertical draft profiles sampled near Darwin, Australia, using 50 MHz profiler data [*Cifelli and Rutledge*, 1998]. In that study, break convection (i.e., tropical continental regime) had significantly larger updrafts in the lower troposphere compared to monsoon convection (i.e., tropical oceanic regime), which was consistent with differences in the respective thermal buoyancy profiles. Sounding data in the Darwin study showed that the break systems occurred in environments with larger positive buoyancy regions compared to the monsoon systems. Results from *Halverson et al*. [2001] suggest that a similar mechanism may be responsible for differences in the convective region vertical draft structure between the easterly and the westerly MCSs in this study.

[39] Note that above the 0°C level, the gradient of both the easterly and the westerly convective vertical air motion profiles decreases, indicating reduced parcel acceleration in this region. This behavior is consistent with the change in corresponding reflectivity gradients (compare Figures 8g and 9g). The main difference between the convective vertical air motion profiles above the melt level is that the easterly (westerly) profile indicates positive acceleration, in the mean, up to ~9.5 (8.0) km. Several studies [*Zipser and Lutz*, 1994; *Petersen et al*., 1999] have suggested that insufficient draft strength at or above the freezing level and an attendant reduction in mixed phase processes are responsible for the lack of lightning in tropical oceanic convection, consistent with observations presented for the westerly regime MCS.

[40] In the WCSF region the main difference in mean vertical air motion structure occurs below 8 km where the easterly MCS shows a larger low-level descent compared to the westerly profile (Figure 9h). The low-level descent in the easterly profile is consistent with corresponding profiles obtained for the trailing portion of several ACSLs sampled during ABLE 2B [*Garstang et al*., 1994]. The lack of mean descent in the

lower portion of the westerly profile is puzzling, given the fact that a relatively pronounced bright band signature is evident in the WCSF mean reflectivity profile (Figure 8e). Many previous studies have shown that mesoscale descending motion below the melting level, associated with the melting of aggregates and evaporation, is a nearly ubiquitous feature of MCS precipitation regions containing a radar bright band [e.g., *Houze*, 1989]. It is possible that the apparent discrepancy is due to errors in the dual-Doppler procedure since the magnitude of the low-level easterly profile is within the mean, accumulated bias of the vertical air motions (i.e., the departure from zero vertical air motion at the ground surface) for this event (not shown). It may also be that the environment of the lower troposphere is more moist in the westerly event, so that evaporation of hydrometeors below the 0°C level is not so significant as compared to the easterly case. It is also possible that despite the bright band signature, weak convection (as opposed to stratiform) is biasing the westerly WCSF kinematic profile. Additional study is needed to test these hypotheses.

[41] The net effect of combining the WCSF and convective vertical air motion profiles (i.e., total category) is to reduce the magnitude of the easterly profile relative to the westerly MCS in the lower troposphere as well as to broaden the region of peak magnitude (Figure 9i;). Also, note the much deeper region of ascent in the easterly case. Because of the correlation between vertical velocity and the apparent heat source [*Yanai et al*., 1973], the differences in the convective vertical air motion structure suggest that corresponding differences exist in the latent heating distribution between these MCSs.

[42] The contours of total mass transport per vertical velocity bin in Figure 9 indicate that the majority of vertical mass transport (defined as the regions enclosed within the 10% relative frequency contour) in both MCSs is accomplished by drafts of moderate intensity (± 3 m s^{-1}), a finding similar to *Yuter and Houze* [1995] for Florida thunderstorms. However, the range of drafts responsible for supporting the mass transport is larger for the 26 January easterly event compared to the 25 February westerly MCS, as evidenced by the magnitude of drafts enclosed within the 1% mass transport relative frequency contour. This result again reflects the increased contribution of intense drafts in the easterly MCS compared to the westerly MCS. Note that the shape of the 1% mass transport per vertical velocity bin contours are slightly wider above 10 km for all precipitation categories in both MCSs, indicating that the intense drafts have the greatest contribution to vertical mass transport in the upper troposphere.

[43] The contours of vertical mass transport also show that the WCSF regions of both MCSs are dynamically active, with a large amount of vertical mass transport from up and down drafts of relatively moderate intensity (± 2 m s^{-1}) (Figures 9b and 9e). However, much of the upward and downward transports cancel in the mean, so the total vertical mass transport (net mass transport for each height level) in the WCSF region is small except at low levels in the easterly case (Figure 10b). The contribution of the WCSF region has a significant impact on the combined profile of total mass transport in the easterly case (Figure 10c). Whereas the convective profiles of total mass transport for both MCSs have peaks near 5 km (Figure 10a), the WCSF contribution causes the peak in the easterly mass transport profile to shift upward and become significantly reduced in magnitude (Figure 10c). In contrast, the combined mass transport profile for the westerly MCS is not much different from the convective profile for this case.

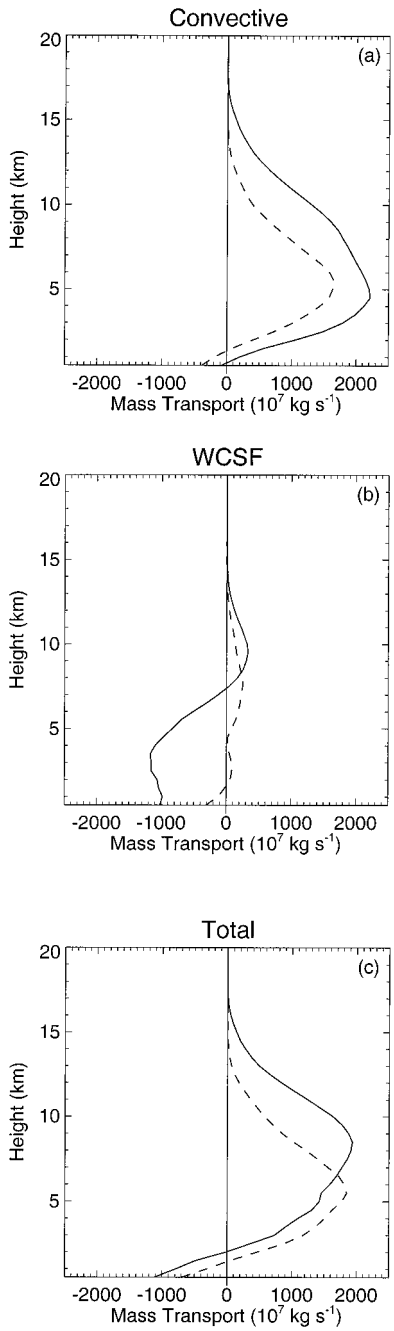

Figure 10. Profiles of total mass transport (10^7 kg s^{-1}) in the (a) convective, (b) WCSF, and (c) total regions of the easterly MCS (solid line) and westerly MCS (dashed line).

[44] The differences in total mass transport for the combined precipitation category are manifestations of life cycle differences in mass transport between the two MCSs (Figure 11). Despite the similarities of life cycle characteristics in terms of low-level reflectivity features shown in Figure 5, these MCSs evidently underwent pronounced differences in terms of kinematic life cycle during their respective sampling periods (Figure 11). The easterly MCS underwent significant changes in terms of kinematic structure during the sampling period, with large positive mass transport occurring throughout the troposphere early-on and negative transport dominating at later stages. In contrast, the westerly MCS, although the intensity

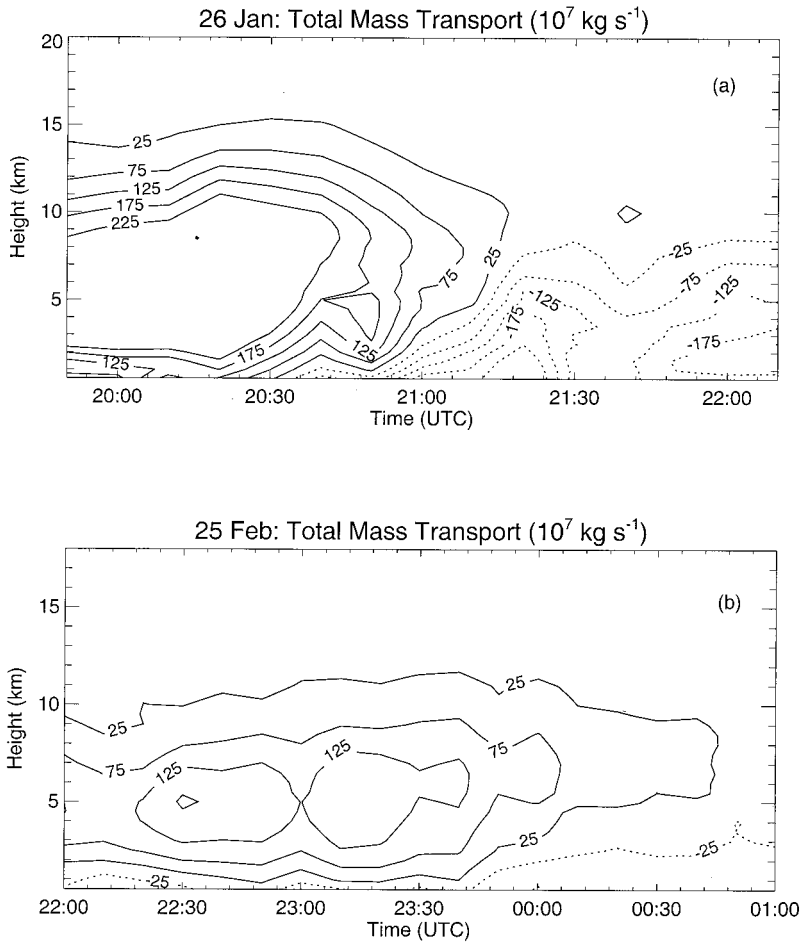

Figure 11. Time-height cross section of total mass transport for the (a) easterly MCS and (b) westerly MCS. Contours are in units of 10^7 kg s^{-1}, starting at 25 and incrementing by 50. Solid (dashed) denotes positive (negative) mass transport.

decreased over time, showed little change in the overall structure of net mass transport characteristics during the sampling period.

4.3.3 Hydrometeor Phase Characteristics

[45] Histograms of liquid and ice water content and mass-weighted mean drop diameter in the mixed phase region (4–8 km) of the two MCSs are shown in Figure 12, while mean profiles of these quantities through the troposphere are shown in Figure 13. Figure 12 shows that the easterly MCS has a higher relative frequency of large ice and water drops in the mixed phase zone compared to the westerly event, which result in larger mean values of these quantities (Figure 13).

[46] It is interesting to compare the frequency of occurrence ratios for precipitation ice versus liquid water mass in the mixed phase region of each MCS (Figures 12a and 12b). For rainwater contents less than ~6 gm m^{-3}, which encompasses the majority of the rain mass distribution, the precipitation ice frequency ratio of easterly to westerly is much larger compared to the same ratio in rain. In fact, for rainwater contents above about 1.7 gm m^{-3}, the ice frequency ratio is infinite. These results are qualitatively consistent with the cross-section analyses of water content (Figure 7) and vertical air motion (Figure 6). Evidently, a significant portion of the rainwater mass in the westerly MCS was not lofted high and/or long enough to be converted into large precipitation ice as evidenced by the large difference in ice mass content between the two systems. The composite easterly MCS vertical draft profile (Figure 9) shows that the magnitude of the drafts in the convective region below the melting level was, on average, a factor of 2 greater than the corresponding drafts in the westerly MCS case. More importantly, the profiles in Figure 9 show that on average, the updrafts in the westerly (easterly) case begin to decelerate at a lower (higher) height above the melting level such that updrafts in the westerly (easterly) case probably could not (could) expose the drops to an environment conducive for accretional growth and resulting formation of large ice particles. A similar feature was noted for selected cells examined during MCTEX [*Carey and Rutledge*, 2000].

[47] The significantly higher precipitation ice mass in the mixed phase region of the easterly MCS is consistent with the higher lightning flash rates in this system compared to the westerly MCS [*Halverson et al*., 2001; *Williams et al*., 2002]. As shown by *Petersen and Rutledge* [2001] and *Baker et al*. [1999], there is a strong correlation between ice water content above the freezing level (7–9 km) and lightning flash density for tropical convection, based on TRMM PR and LIS observations for selected regions in the global tropics. A similar correlation was found between polarimetric radar-inferred precipitation ice mass and total flash rate in tropical island thunderstorms

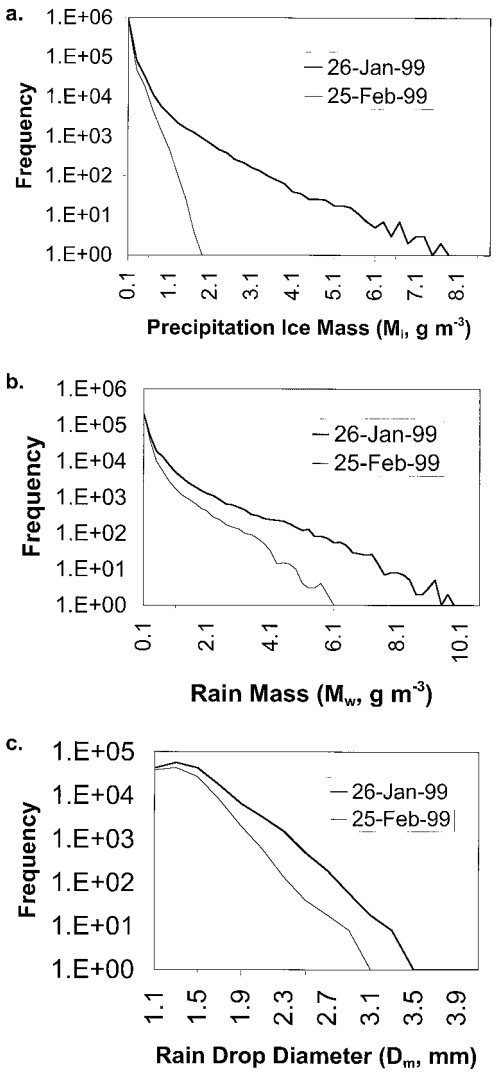

Figure 12. Frequency histograms of precipitation characteristics in the mixed phase zone (4–8 km) as derived from S-pol observations of horizontal and differential reflectivity. (a) Precipitation ice mass (M_i, gm m^{-3}), (b) rain mass (M_w, gm m^{-3}), and (c) mass-weighted mean raindrop diameter (D_m, mm). The bin size in each plot is 0.2, starting at 0.1 in (a) and (b) and 1.1 in (c).

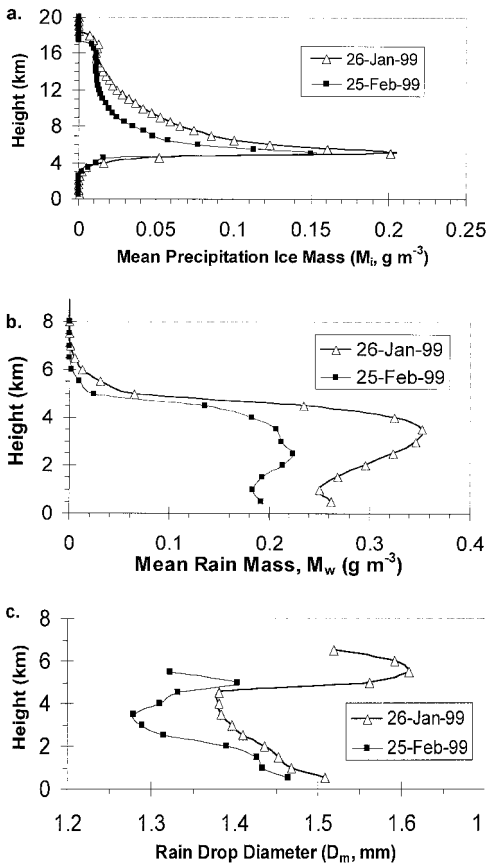

Figure 13. Vertical profiles of mean precipitation characteristics as determined from S-pol observations of horizontal and differential reflectivity. (a) Precipitation ice mass (M_i, gm m^{-3}), (b) rain mass (M_w, gm m^{-3}), and (c) mass-weighted mean drop diameter (D_m, mm). Note that M_w in (a) is an unconditional mean, while D_m in (c) is a conditional mean (i.e., M_w must be > 0). D_m is plotted at all altitudes where $M_w > 0.005$.

[*Ahijevych et al.*, 2000; *Carey and Rutledge*, 2000]. Results shown in Figures 12 and 13 further suggest that ice microphysics probably played a more important role in rainfall production for the easterly MCS compared to the westerly MCS. Because emission and scattering characteristics at microwave frequencies are sensitive to the vertical distribution of ice and liquid water within the cloud, these results have important implications for TRMM algorithms which utilize passive microwave sensors to infer rainfall and latent heating structure [e.g., *Fulton and Heymsfield*, 1991; *Kummerow et al.*, 1996; *Olson et al.*, 1999; *Yang and Smith*, 1999; *Bauer et al.*, 2000].

[48] Figures 12 and 13 also show that mean drop size (D_m) in the easterly MCS is larger compared to the westerly MCS. The offset in the peak D_m above the melting level (Figure 13c) probably reflects the corresponding offset in peak drop collision-coalescence as a consequence of the differences in updraft strength described above. Below the melting level, the larger average D_m in the easterly MCS is consistent with surface disdrometer observations collected during TRMM LBA (A. Tokay, personal communication, 2000). The reason for the offset below the melt level is not obvious but may represent differences in the density of hydrometeors lofted above the freezing level which subsequently fall out of the updraft and melt (with different water equivelent diameters). Specifically, in the mean the differences in D_m may reflect the melting of aggregates or soft graupel in the westerly case versus graupel or hail in the easterly case.

4.3.4 Rainfall Characteristics

[49] Composite histograms of the average rain rate for the easterly and westerly events are shown in Figure 14. The distributions at low rain rates (<5 mm h^{-1}) are almost identical for these MCSs; however, as expected from the analyses presented above, the easterly MCS has a higher frequency of occurrence of intense rain rates. These intense but infrequent rain rates in the easterly case have a large impact on the average rain rate for the MCS sampling periods. This is evidenced by the fact that the mean rain rate is approximately a factor of 2 larger in the easterly MCS compared to the westerly MCS. Taken together with the reflectivity and ice water content results shown in Figures 8 and 12, the rain rate results are

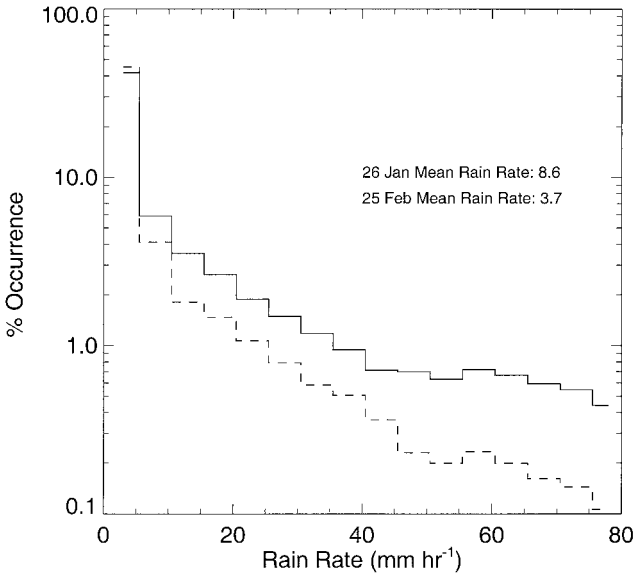

Figure 14. Composite rain rate histogram for the easterly event (solid line) and westerly event (dashed line). The average rain rate (mm h^{-1}) for each MCS is indicated. The rain rate histograms were generated using a 2 mm h^{-1} bin size.

consistent with *DeMott and Rutledge* [1998a] and *Petersen and Rutledge* [2001], showing that for the west Pacific warm pool region and the global tropics as a whole, larger rain rates are well correlated to larger fractions of reflectivity area exceeding 30 dBZ and larger ice water contents in the mixed phase region. Similar results were also found in MCTEX [*Carey and Rutledge*, 2000]. In that study, mixed phase ice mass and rainfall increased by a factor of 2–3 above the associated increase in low-level echo area during an upscale development of tropical island convection. This enhancement in precipitation production was well correlated with the production of lightning.

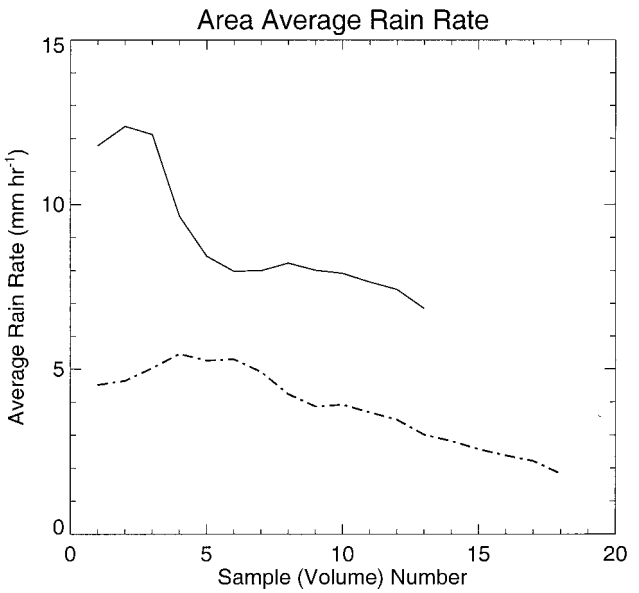

Figure 15. Time series of average rain rate for the easterly event (solid line) and westerly event (dashed line). The absicca represents the radar volume number instead of time, so the two series can be overlaid.

[50] A time series of the average rain rate for each system is shown in Figure 15. As expected, the easterly rain rates are larger, on average, compared to the westerly case. Both systems show an overall intensity reduction of about a factor of 2 during their respective sampling periods. The major difference is that the easterly time series shows that the area average rain rate had two periods of relatively steady rain intensity separated by a short period of rapidly decreasing rain rate. This trend is consistent with the change in kinematic structure (i.e., mass transport) shown in Figure 11. In contrast, the westerly MCS area average rain rate slowly decreases over time with no obvious transition identifying a particular stage of life cycle evolution.

5. Summary

[51] Two MCSs have been analyzed using dual-Doppler and multiparameter radar data collected during TRMM LBA. The MCSs occurred in distinct meteorological regimes (easterly versus westerly low-level flow), based on atmospheric sounding data. Approximately 2.5–3.0 hours of dual Doppler data were analyzed for each MCS. The radar data were partitioned into convective and WCSF components in order to assess the relative kinematic and microphysical contributions of each precipitation category.

[52] Analysis of the radar data showed that the MCSs had pronounced differences in terms of vertical structure and rainfall characteristics. By all measures used to compare the MCSs (vertical air motion, vertical mass transport, reflectivity, water content, and rainfall), the easterly event was more intense in terms of kinematic and microphysical features. This suggests that during TRMM LBA, at least two distinct types of convective vertical structure were observed. The easterly system was characterized by intense updrafts and a well-developed reflectivity structure above the freezing level, similar to tropical continental convection documented elsewhere. Polarimetric data showed evidence for an active mixed phase microphysical zone with hail production and significant precipitation ice generation. In terms of kinematic characteristics the easterly MCS had a significant contribution from WCSF echo regions, especially in the lower troposphere, which affected the overall shape of the kinematic profile (as measured in terms of vertical air motion and mass transport).

[53] In contrast, the westerly MCS was weaker in terms of overall kinematic and reflectivity structure, and its organization was more complicated, similar to monsoon convection observed elsewhere in the tropics. Despite some evidence for liquid water being lofted to heights above the melting level, precipitation-sized ice production in the mixed phase zone (4–8 km) was significantly less compared to the easterly MCS, suggesting that the vertical drafts were not strong enough to levitate liquid drops high and/or long enough for significant freezing to occur. In contrast to the easterly MCS the westerly MCS showed a featureless life cycle effect in terms of kinematic structure or area average rainfall rate.

[54] These results have important implications for TRMM since accurate characterization of diabatic heating profiles across the global tropics, a major goal of the TRMM program, is directly coupled to the kinematic and microphysical structure in precipitating convection. Moreover, it is hoped that these observations can provide validation for numerical models

and passive microwave algorithms that will be used to estimate latent heating in the tropical atmosphere of the Amazon for TRMM. Future research will focus on a statistical analysis of the vertical structure of the numerous precipitation features observed during TRMM LBA to determine the magnitude of differences between the east and the west regime across the entire spectrum of sampled convection.

[55] **Acknowledgments.** We thank Earle Williams and an anonymous reviewer for suggestions on improving the manuscript. This research was supported by NASA TRMM grant NAG5-4754. TRMM LBA was supported by the NASA TRMM program under the direction of R. Kakar. Partial support for the S-pol radar was provided by the National Science Foundation. Otto Thiele of the NASA TRMM Office was instrumental in setting up the TRMM-LBA program and making it a success. Discussions with Tom Rickenbach and Jeff Halverson were helpful in placing the radar observations in context of the large-scale environment. Ali Tokay provided disdrometer-derived *Z-R* relations that were used in the rainfall analysis. Paul Hein provided valuable computer support. Appreciation is extended to all the participants of TRMM LBA who helped make the field program a success.

References

Ahijevych, D. A., S. A. Rutledge, and L. D. Carey, Radar and electrical characteristics of convection observed during MCTEX, *Aust. Meteorol. Mag*., *49*, 165–180, 2000.

Baker, M. B., A. M. Blyth, H. J. Christian, J. Latham, K. L. Miller, and A. M. Gadian, Relationships between lightning activity and various thundercloud parameters: Satellite and modelling studies, *Atmos. Res*., *51*, 221–236, 1999.

Balakrishnan, N., and D. S. Zrnic′, Estimates of rain and hail rates in mixed-phase precipitation, *J. Atmos. Sci*., *47*, 565–583, 1990.

Bauer, P., A. Khain, A. Pokrovsky, R. Meneghini, C. Kummerow, F. Marzano, and J.P.V. Poiares Baptista, Combined cloud-microwave radiative transfer modeling of stratiform rainfall, *J. Atmos. Sci*., *57*, 1082–1104, 2000.

Bringi, V. N., and V. Chandrasekar, *Polarimetric Doppler Weather Radar—Principles and Applications*, 636 pp., Cambridge Univ. Press, New York, 2001.

Bringi, V. N., K. Knupp, A. Detwiler, L. Liu, I. J. Caylor, and R. A. Black, Evolution of a Florida thunderstorm during the Convection and Precipitation/Electrification Experiment: The Case of 9 August 1991, *Mon. Wea. Rev*., *125*, 2131–2160, 1997.

Carey, L. D., and S. A. Rutledge, The relationship between precipitation and lightning in tropical island convection: A C-band polarimetric radar study, *Mon. Weather Rev*., *128*, 2687–2710, 2000.

Carey, L. D., S. A. Rutledge, D. A. Ahijevych, and T. D. Keenan, Correcting propagation effects in C-band polarimetric radar observations of tropical convection using differential propagation phase, *J. Appl. Meteorol*., *39*, 1405–1433, 2000a.

Carey, L. D., R. Cifelli, W. A. Petersen, and S. A. Rutledge, Preliminary report on TRMM-LBA rainfall estimation using the S-POL radar, *Tech. Rep*. *697*, 19 pp., Dep. of Atmos. Sci. Colo. State Univ., 2000b.

Chandrasekar, V., E. Gorgucci, and G. Scarchilli, Optimization of multi-parameter radar estimates of rainfall, *J. Appl. Meteorol*., *32*, 1288–1293, 1993.

Cheng, C.-P., and R. A. Houze Jr., The distribution of convective and mesoscale precipitation in GATE radar echo patterns, *Mon. Weather Rev*., *107*, 1370–1381, 1979.

Cifelli, R., and S. A. Rutledge, Vertical motion structure in Maritime Continent mesoscale convective systems: Results from a 50-MHz profiler, *J. Atmos. Sci*., *51*, 2631–2652, 1994.

Cifelli, R., and S. A. Rutledge, Vertical motion, diabatic heating, and rainfall characteristics in N. Australia convective systems, *Q. J. R. Meteorol. Soc*., *124*, 1133–1162, 1998.

DeMaria, M., Linear response of a stratified tropical atmosphere to convective forcing, *J. Atmos. Sci*., *42*, 113–121, 1985.

DeMott, C. A., and S. A. Rutledge, The vertical structure of TOGA COARE convection, part I, Radar echo distributions, *J. Atmos. Sci*., *55*, 2730–2747, 1998a.

Demott, C. A., and S. A. Rutledge, The vertical structure of TOGA COARE convection, part II, Modulating influences and implications for diabatic heating, *J. Atmos. Sci*., *55*, 2748–2762, 1998b.

Doviak, R. J., and D. S. Zrnic′, *Doppler Radar and Weather Observations*, 2nd ed., 562 pp., Academic, San Diego, Calif., 1993.

Ferrier, B. S., W. K. Tao, and J. Simpson, A double-moment multiple-phase four-class bulk ice scheme, part II, Simulations of convective storms in different large-scale environments and comparisons with other bulk parameterizations, *J. Atmos. Sci*., *52*, 1001–1033, 1995.

Fulton, R., and G. M. Heymsfield, Microphysical and radiative characteristics of convective clouds during COHMEX, *J. Appl. Meteorol*., *30*, 98–116, 1991.

Gandu, A. W., and P. L. Silva Dias, Impact of tropical heat sources on the South American tropospheric upper circulation and subsidence, *J. Geophys. Res*., *103*, 6001–6015, 1998.

Garstang, M., et al., The Amazon Boundary Layer Experiment (ABLE 2B): A meteorological perspective, *Bull. Am. Meteorol. Soc*., *71*, 19–32, 1990.

Garstang, M., H. L. Massie Jr., J. Halverson, S. Greco, and J. Scala, Amazon coastal squall lines, part I, Structure and kinematics, *Mon. Weather Rev*., *122*, 608–622, 1994.

Golestani, Y., V. Chandrasekar, and V. N. Bringi, Intercomparison of multiparameter radar measurements in *Proceedings of 24th Conference on Radar Meteorology*, pp. 309–314, Am. Meteorol. Soc., Boston, Mass., 1989.

Goodman, S. J., D. E. Buechler, P. D. Wright, and W. D. Rust, Lightning and precipitation history of a microburst-producing storm, *Geophys. Res. Lett*., *15*, 1185–1188, 1988.

Greco, S., R. Swap, M. Garstang, S. Ulanski, M. Shipham, R. C. Harriss, R. Talbot, M. O. Andreae, and P. Artaxo, Rainfall and surface kinematic conditions over central Amazonia during ABLE 2B, *J. Geophys. Res*., *95*, 17,001–17,014, 1990.

Greco, S., J. Scala, J. Halverson, H. L. Massie Jr., W. K. Tao, and M. Garstang, Amazon coastal squall lines, part II, Heat and moisture transports, *Mon. Weather Rev*., *122*, 623–635, 1994.

Halverson, J. B., T. Rickenbach, B. Roy, H. Pierce, and E. Williams, Environmental characteristics of convective systems during TRMM-LBA, *Mon. Weather Rev.*, *130*, 1493–1509, 2001.

Hartmann, D. L., H. H. Hendon, and R. A. Houze Jr., Some implications of the mesoscale circulations in tropical cloud clusters for large-scale dynamics and climate, *J. Atmos. Sci*., *41*, 113–121, 1984.

Harriss, R. C., et al., The Amazon Boundary Layer Experiment: Wet season 1987, *J. Geophys. Res*., *95*, 16,721–16,736, 1990.

Herzegh, P. H., and A. R. Jameson, Observing precipitation through dual-polarization radar measurements, *Bull. Am. Meteorol. Soc*., *73*, 1365–1374, 1992.

Houze, R. A., Jr., Cloud clusters and large-scale vertical motions in the tropics, *J. Meteorol. Soc. Jpn*., *60*, 396–409, 1982.

Houze, R. A., Jr., Observed structure of mesoscale convective systems and implications for large-scale heating, *Q. J. R. Meteorol. Soc*., *115*, 425–461, 1989.

Hubbert, J., and V. N. Bringi, An iterative filtering technique for the analysis of copolar differential phase and dual-frequency radar measurements, *J. Atmos. Oceanic Technol*., *12*, 643–648, 1995.

Jameson, A. R., M. J. Murphy, and E. P. Krider, Multiple-parameter radar observations of isolated Florida thunderstorms during the onset of electrification, *J. Appl. Meteorol*., *35*, 343–354, 1996.

Johnson, R. H., and G. S. Young, Heat and moisture budgets of tropical mesoscale anvil clouds, *J. Atmos. Sci*., *40*, 2138–2147, 1983.

Jorgensen, D. P., and M. A. LeMone, Vertical velocity characteristics of oceanic convection, *J. Atmos. Sci*., *46*, 621–640, 1989.

Keenan, T. D., and R. E. Carbone. A preliminary morphology of precipitation systems in tropical northern Australia, *Q. J. R. Meteorol. Soc*., *118*, 283–326, 1992.

Kousky, V. E., Diurnal rainfall variation in northeast Brazil, *Mon. Weather Rev*., *108*, 488–498, 1980.

Kummerow, C., and L. Giglio, A passive microwave technique for estimating rainfall and vertical structure information from space, part I, Algorithm description, *J. Appl. Meteorol*., *33*, 3–18, 1994a.

Kummerow, C., and L. Giglio, A passive microwave technique for estimating rainfall and vertical structure information from space, part II, Applications to SSM/I data, *J. Appl. Meteorol*., *33*, 19–34, 1994b.

Kummerow, C., W. S. Olson, and L. Giglio, A simplified scheme for obtaining preciptiation and vertical hydrometeor profiles from passive microwave sensors, *IEEE Trans. Geosci. Remote Sens*., *34*, 1213–1232, 1996.

Leary, C. A., and R. A. Houze Jr., The structure and evolution of convection in a tropical cloud cluster, *J. Atmos. Sci*., *36*, 437–457, 1979.

Lin, X., and R. H. Johnson, Heat and moisture budgets and circulation characteristics of a frontal squall line, *J. Atmos. Sci*., *51*, 1661–1681, 1994.

Mapes, B., and R. A. Houze Jr., Diabatic divergence profiles in western Pacific mesoscale convective systems, *J. Atmos. Sci*., *52*, 1807–1828, 1995.

Mohr, C. G., and L. J. Miller, CEDRIC — A software package for cartesian space editing, synthesis, and display of radar fields under interactive control in *Preprints of 21st Conference on Radar Meteorology*, pp. 559–574, Am. Meteorol. Soc., Boston, Mass., 1983.

Mohr, C. G., L. J. Miller, R. L. Vaughan, and H. W. Frank, The merger of mesoscale data sets into a common cartesian format for efficient and systematic analyses, *J. Atmos. Oceanic Technol*., *3*, 143–161, 1986.

Molion, L. C. B., On the dynamic climatology of the Amazon Basin and associated rain producing mechanisms, in *Geophysiology of Amazonia Vegetation and Climate Interactions*, edited by R. E. Dickenson, pp. 391–407, John Wiley, New York, 1987.

Nesbitt, S. W., E. J. Zipser, and D. J. Cecil, A census of precipitation features in the tropics using TRMM: Radar, ice scattering and lightning observations, *J. Clim*., *13*, 4087–4106, 2000.

O'Brien, J. J., Alternative solutions to the classical vertical velocity problem, *J. Appl. Meteorol*., *9*, 197–203, 1970.

Olson, W. S., C. D. Kummerow, Y. Hong, and W. K. Tao, Atmospheric latent heating distributions in the Tropics derived from satellite passive microwave radiometer measurements, *J. Appl. Meteorol*., *38*, 633–664, 1999.

Oye, R., and R. E. Carbone, Interactive Doppler editing software, in *Proceedings of 20th Conference on Radar Meteorology*, pp. 683–689, Am. Meteorol. Soc., Boston, Mass. 1981.

Petersen, W. A., and S. A. Rutledge, On the relationship between cloud-to-ground lightning and convective rainfall, *J. Geophys. Res*., *103*, 14,025–14,040, 1998.

Petersen, W. A., and S. A. Rutledge, Regional variability in tropical convection: Observations from TRMM, *J. Clim*., *14*, 3566–3586, 2001.

Petersen, W. A., L. D. Carey, S. A. Rutledge, J. C. Knievel, N. J. Doesken, R. H. Johnson, T. B. McKee, T. Vonder Haar, and J. F. Weaver, Mesoscale and radar observations of the Fort Collins flash flood of 28 July 1997, *Bull. Am. Meteorol. Soc*., *80*, 191–216, 1999.

Petersen, W. A., S. W. Nesbitt, R. J. Blakeslee, R. Cifelli, P. Hein, and S. A. Rutledge, TRMM observations of convective regimes in the Amazon. *J. Clim.*, in press, 2001.

Rickenbach, T. M., and S. A. Rutledge, Convection in TOGA COARE: Horizontal scale, morphology, and rainfall production, *J. Atmos. Sci*., *55*, 2715–2729, 1998.

Rickenbach, T. M., R. N. Ferreira, J. Halverson, and M.A.F. Silva Dias, Modulation of convection in the southwestern Amazon basin by extratropical stationary fronts, *J. Geophys. Res*., *107*, doi:10.1029/2000JD000263, in press, 2002.

Rogers, R. R., A review of multiparameter radar observations of precipitation, *Radio Sci*., *19*, 23–36, 1984.

Rutledge, S. A., E. R. Williams, and T. D. Keenan, The Down Under Doppler and Electricity Experiment (DUNDEE): Overview and preliminary results, *Bull. Am. Meteorol. Soc*., *73*, 3–16, 1992.

Rutledge, S. A., W. A. Petersen, R. Cifelli, and L. D. Carey, Early results from TRMM-LBA: Kinematic and microphysical characteristics of convection in distinct meteorological regimes in *Proceedings of 24th Conference on Hurricanes and Tropical Meteorology*, pp. 137–138, Am. Meteorol. Soc., Boston, Mass., 2000.

Ryzhkov, A. V., and D. S. Zrnic′, Comparison of dual-polarization radar estimators of rain, *J. Atmos. Oceanic Technol*., *12*, 249–256, 1995.

Ryzhkov, A. V., and D. S. Zrnic′, Polarimetric rainfall estimation in the presence of anomalous propagation. *J. Atmos. Oceanic Technol*., *15*, 1320–1330, 1998.

Scala, J. R., M. Garstang, W. K. Tao, K. E. Pickering, A. M. Thompson, J. Simpson, V.W.J.H. Kiirchhoff, E. V. Browell, G. W. Sachse, A. L. Torres, G. L. Gregory, R. A. Rasmussen, and M. A. K. Khalil, Cloud draft structure and trace gas transport. *J. Geophys. Res*., *95*, 17,015–17,030, 1990.

Silva Dias, M., et al., Clouds and rain processes in a biosphere atmosphere interaction context in the Amazon region, *J. Geophys. Res*., *107*, 10.1029/2001JD000335, in press, 2002.

Simpson, J., R. F. Adler, and G. R. North, A proposed Tropical Rainfall Measuring Mission (TRMM) satellite, *Bull. Am. Meteorol. Soc*., *69*, 278–295, 1988.

Smith, P. L., D. J. Musil, A. G. Detwiler, and R. Ramachandran, Observations of mixed-phase precipitation within a CaPE thunderstorm, *J. Appl. Meteorol*., *38*, 145–155, 1999.

Steiner, M., R. A. Houze Jr., and S. E. Yuter, Climatological characteristics of three-dimensional storm structure from operational radar and rain gauge data, *J. Appl. Meteorol*., *34*, 1978–2007, 1995.

Straka, J. M., D. S. Zrnic', and A. V. Ryzhkov, Bulk hydrometeor classification and quantification using polarimetric radar data: Synthesis of relations, *J. Appl. Meteorol*., *39*, 1341–1372, 2000.

Szoke, E. J., E. J. Zipser, and D. P. Jorgensen, A radar study of convective cells in mesoscale systems in GATE, part I, Vertical profile statistics and comparison with hurricanes, *J. Atmos. Sci*., *43*, 182–197, 1986.

Takahashi, T., and K. Kuhara, Precipitation mechanisms of cumulonimbus clouds at Pohnpei, Micronesia, *J. Meteorol. Soc. Jpn*., *71*, 21–31, 1993.

Tao, W. K., J. Simpson, S. Lang, M. McCumber, R. Adler, and R. Penc, An algorithm to estimate the heating budget from vertical hydrometeor profiles, *J. Appl. Meteorol*., *29*, 1232–1244, 1990.

Tao, W. K., J. Simpson, C. H. Sui, B. Ferrier, S. Lang, J. Scala, M. D. Chou, and K. Pickering, Heating, moisture, and water budgets of tropical and middle latitude squall lines: Comparisons and sensitivity to longwave radiation, *J. Atmos. Sci*., *50*, 673–690, 1993.

Williams, E. R., S. A. Rutledge, S. C. Geotis, N. Renno, E. Rasmussen, and T. Rickenbach, A radar and electrical study of tropical hot towers, *J. Atmos. Sci*., *49*, 1386–1395, 1992.

Williams, E., et al., The green ocean over the Amazon: Implications for cloud electrification, *J. Geophys. Res*., *107*, 10.1029/2001JD000380, in press, 2002.

Yanai, M., S. Esbensen and J. H. Chu, Determination of bulk properties of tropical cloud clusters from large-scale heat and moisture budgets, *J. Atmos. Sci*., *30*, 611–627, 1973.

Yang, S., and E. A. Smith, Four-dimensional structure of monthly latent heating from SSM/I satellite measurements, *J. Clim*., *12*, 1016–1037, 1999.

Yuter, S. E., and R. A. Houze Jr., Three-dimensional kinematic and microphysical evolution of Florida cumulonimbus, part III, Vertical mass transport, mass divergence, and synthesis, *Mon. Weather Rev*., *123*, 1964–1983, 1995.

Zipser, E. J., Deep cumulonimbus cloud systems in the tropics with and without lightning, *Mon. Weather Rev*., *122*, 1837–1851, 1994.

Zipser, E. J., and K. Lutz, The vertical profile of radar reflectivity of convective cells: A strong indicator of storm intensity and lightning probability? *Mon. Weather Rev*., *122*, 1751–1759, 1994.

Zipser, E. J., R. J. Meitin, and M. A. LeMone, Mesoscale motion fields in association with a GATE convection band, *J. Atmos. Sci*. *38*, 1725–1750, 1981.

Zrnic′, D. S., and A. Ryzhkov, Advantages of rain measurements using specific differential phase, *J. Atmos. Oceanic Technol*. *13*, 454–464, 1996.

L. D. Carey, R. Cifelli, W. A. Petersen, and S. A. Rutledge, Department of Atmospheric Science, Colorado State University, Fort Collins, CO 80523-1371, USA. (rob@radarmet.atmos.colostate.edu)

M. A. F. da Silva Dias, Department of Atmospheric Science, University of São Paulo, São Paulo, Brazil.